The Effect of Thickness-Tunable ZrO₂ Shell on Enhancing the Tunneling Magnetoresistance of Fe₃O₄ Supraparticles

Shu Mi, Yong Xie,* Yuanyuan Li, Rui Liu, Xiaoduo Liu, Ivan I. Smalyukh, and Ziyu Chen*

The core–shell Fe₃O₄@ZrO₂ nanoparticles with controllable shell thickness and core dimensions are synthesized using solvothermal approaches. The introduction of the insulator ZrO₂ shell allows realizing the enhancement of tunneling magnetoresistance (TMR) effect of the functional nanomaterials. The influences of temperature, magnetic field, and shell thickness on the TMR are explored. With the shell thickness ≈3 nm TMR ratio of 10% is obtained, which improves the MR compared to the pure Fe₃O₄ counterpart of 5.7%. Furthermore, the MR is increased first and then decreases with increase of the shell thickness, which suggests that the addition of insulated shell-layer promotes the electron tunneling among the supraparticles and thereby increases the MR. The fault-cutting data indicate that the tunneling mechanism occurs mainly through the magnetic-insulator interfaces rather than the interior nanoparticle interfaces. In addition, the MR with different core-size presents a monotonic increase with decrease of the size of core.

1. Introduction

Half-metallic magnetite Fe₃O₄ has been a promising candidate for performing large tunneling magnetoresistance (TMR) due to its nearly 100% spin polarization and the known highest Curie temperature of 860 K.[1–3] In theory, a high spin polarization should result in a large TMR, which is proportional to the spin polarization of tunneling electrons.[4–6] Based on this idea, various kinds of magnetite and their TMR properties have been explored in the last decades, including single crystal,[7] epitaxial, and polycrystal films,[8–10] tunneling junctions,[3,11–13] and granular systems.[14–17] However, in most cases the magnetoresistance (MR) ratio is smaller than expected, especially

S. Mi, Dr. Y. Xie, Y. Y. Li, R. Liu, X. D. Liu, Prof. Z. Y. Chen
Department of Physics
Beihang University
Beijing 100191, China
E-mail: xiey@buaa.edu.cn; chenzy@buaa.edu.cn
Prof. I. I. Smalyukh
Department of Physics
Material Science and Engineering Program
Department of Electrical
Computer
and Energy Engineering
and Liquid Crystal Materials Research Center
University of Colorado
Boulder, CO 80309, USA

The ORCID identification number(s) for the author(s) of this article can be found under https://doi.org/10.1002/admi.201800236.

at room temperature. This degradation is caused admittedly by the reduced spin polarization due to the multiple effects of oxidation, defects, bonding, and surface reconstruction at the surfaces or interfaces of the polycrystal grain boundaries. Comparing to bulk materials, the nanoparticles can produce enhanced extrinsic MR owing to the effect of spin-dependent interface scattering or tunneling through the boundaries.[18] Additionally, the MR can still be increased by core–shell encapsulated structures. For example, an insulating shell coats on the magnetite core. In such a dielectric system, nanometric ferromagnetic particles show giant TMR by spin-dependent tunneling of conducting electrons at the magnetic-insulator interfaces. Electrons with spin parallel to the particle magnetization have a bigger probability of tunneling than electrons with antiparallel spin, resulting in an overall lower resistance. Similar MR enhancement has been realized in Fe₃O₄@SiO₂,[19] Fe₃O₄@ oleic acid,[20] Fe@Cr,[21] and Fe₃O₄@ZnS[22] system. Insulator zirconium dioxide (ZrO₂) is a nonmetallic inorganic material and has excellent resistance to acids and alkalis. It was widely applied in catalyst carrier and thermal barrier fields due to the stability and insulativity. Previous studies have shown that ZrO₂ doping in the perovskite systems can effectively enhance the magnetoresistance.[23–25] To the best of our knowledge, it is still unexploited of ZrO₂ doping in the half-metal Fe₃O₄ nanoparticles by means of the core–shell structural system.

In this paper, Fe₃O₄@ZrO₂ core–shell nanocomposites are prepared with controllable shell thickness and core–size. The pomegranate-like core is obtained and composed of several monocrystals and single-domain Fe₃O₄ nanocrystals with size <10 nm. The magnetic structure and magnetotransport property of the core–shell nanocomposites are explored. Our results show that the MR is increased to ≈7.5% at 2 kOe in this core–shell system compared to that of pure Fe₃O₄ nanoparticles ≈4.7%. Moreover, as Zr content increases, the MR first increases and then decreases. This is because the addition of insulated barrier promotes the tunneling effect, which enhances the MR, but with further increase of ZrO₂ thickness, the barrier becomes larger and the electron tunneling becomes difficult, leading to the reduced MR. In addition, the results of Fe₃O₄@ZrO₂ with different core sizes show that the MR rises monotonically with a decrease of the size of core. Moreover, for eliminate the possible effect of ZrO₂ permeating into the interior of the pomegranate-like core, fault-cutting is prepared and

**ADVANCED
SCIENCE NEWS**
www.advancedsciencenews.com

**ADVANCED
MATERIALS
INTERFACES**
www.advmatinterfaces.de

examined by transmission electron microscopy (TEM) imaging and element mapping. ZrO_2 component is little within the core, indicating tunneling occurs mainly through the magnetic-insulator interfaces. This kind of core–shell magnetic nanocomposites would be a promising material applicable in the next-generation spintronic devices. Our research will also be helpful to guide the enhancement of the MR in magnetic nanoparticle systems and to understand electron tunneling magnetotransport mechanism behind the advanced nanocomposite materials.

2. Results and Discussion

The Fe_3O_4 supraparticles were synthesized by a modified solvothermal approach by reduction of $FeCl_3$ with ethylene glycol (see the Experimental Section). The magnetite supraparticles have a uniform size of about 260 nm and spherical shape as shown in TEM image (**Figure 1**a). High magnification TEM image (Figure 1a, top-right inset) shows that the obtained magnetite supraparticles are pomegranate-like clusters with distinguishable nanocrystals size <10 nm in the early as-synthesized stage. The high-resolution TEM (HRTEM) image

reveals that the crystalline grains are monocrystals and single-domain Fe_3O_4 nanoparticles. The measured lattice spacing of 0.24 nm corresponds to the (222) plane of the cubic phase of Fe_3O_4 with a space group of *Fd-3m* as shown in Figure 1a, bottom inset. By X-ray diffraction (XRD) spectrum (Figure S1, Supporting Information), the Fe_3O_4 nanoparticles are evaluated with an average grain size of about 11 nm based on the Debye–Scherrer formula.[26] Figures S1b and S2 of the Supporting Information show further the superparamagnetism and MR value of 6.5% of the as-synthesized Fe_3O_4 supraparticles. **Figure 2** shows the detailed formation mechanism of the ZrO_2 shell coated on the Fe_3O_4. Sodium citrate was added first into the Fe_3O_4 solution to prevent aggregation by the adsorbed Cit^{3-} charged ions (Figure 2, step 1 and 2). Fe_3O_4 supraparticles were then added to solution obtained by dissolving zirconium isopropoxide (Zr-isop.) in ethanol as schematic in Figure 2, step 3. Exchange reaction occurs between Zr-isop. and ethanol. Then Zr-intermediate reactant was further hydrolyzed to form the amorphous ZrO_2 adsorbed on the surface of Fe_3O_4 particles electrostatically (Figure 2, step 4). In this process, the shell thickness can be tuned by varying the molar ratio of reactants. After annealing at 723 K, the crystalline ZrO_2 and overgrown Fe_3O_4 grains were obtained as shown in Figure 2, step
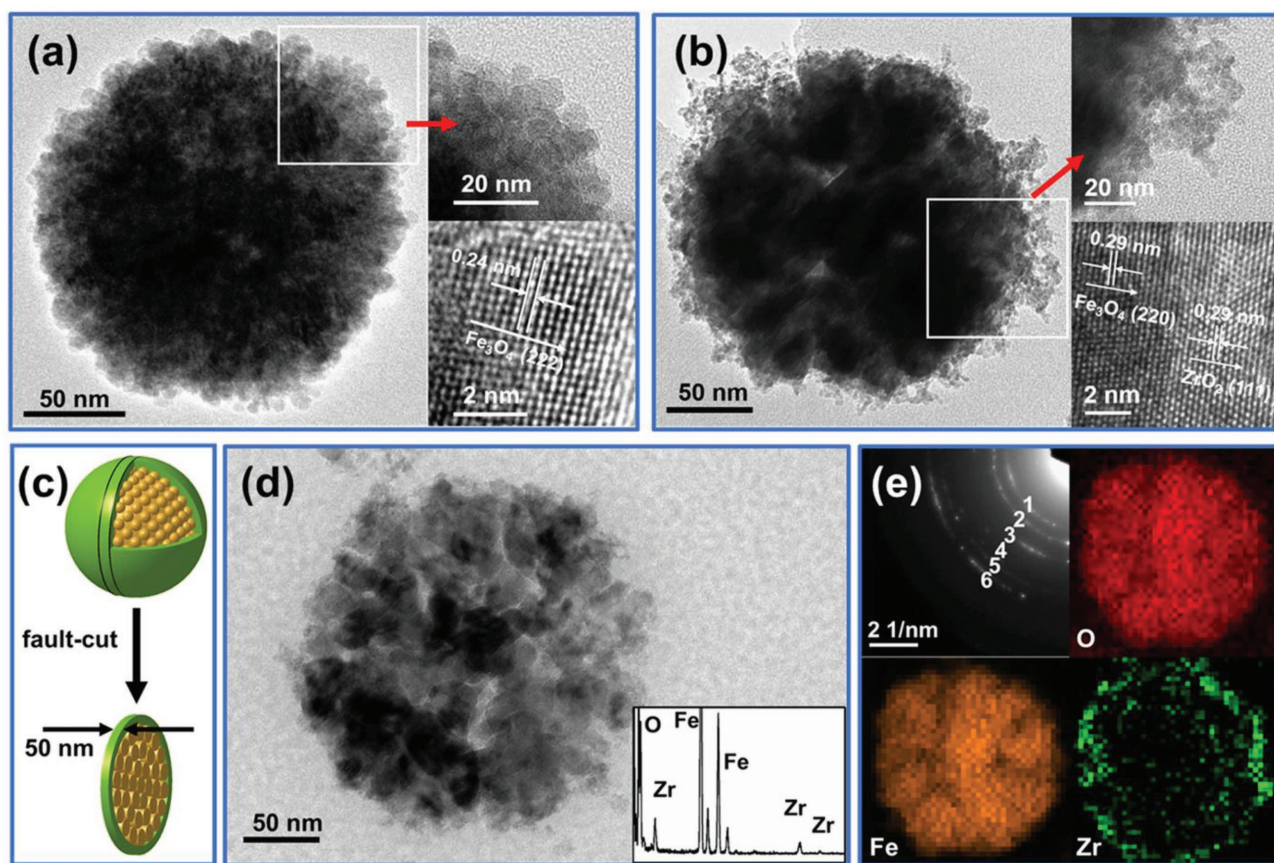
Figure 1. TEM image of a) the as-prepared Fe_3O_4 supraparticle and b) the annealed $Fe_3O_4@ZrO_2$ supraparticle, the insets of (a) and (b) show the high magnification TEM and HRTEM, respectively. c) A brief illustration showing the fault-cutting process. The green parts are the ZrO_2 shell and the yellow parts show the Fe_3O_4 nanocrystals. d) TEM image and energy dispersive spectrum (EDS) (the inset) of the fault-cutting slice. e) The corresponding selected area electron diffraction (SAED) and EDS elemental mapping of (d).

Figure 2. Schematic illustration of the formation processes of $Fe_3O_4@ZrO_2$ core–shell nanocomposite (see text for details in step 1–5).

5 and confirmed by TEM images of Figure 1b. The size of the annealed $Fe_3O_4@ZrO_2$ supraparticles is no noticeable change. The high-magnification TEM and HRTEM (Figure 1b insets) show the detectable lattice interface between the Fe_3O_4 core and the ZrO_2 shell, which suggests an epitaxial crystallization of the ZrO_2 layer on the surface of Fe_3O_4 nanoparticles because of the high lattice-match between the (220) plane of Fe_3O_4 and the (111) plane of ZrO_2 as shown in Figure 1b, the HRTEM and **Figure 3**a, the XRD. The elements maps of the core–shell $Fe_3O_4@ZrO_2$ are further shown in Figure S3 of the Supporting Information.

To probe the possibility of ZrO_2 elements permeating into the Fe_3O_4 supraparticles, which may cause the uncertainty of MR measurements, fault-cutting slice was prepared to make sure the in-plane distribution of the ZrO_2 shell. Figure 1c presents first a schematic to describe the fault-cutting processes, in which the thickness of the slice is controlled at around 50 nm. Figure 1d and Figure S4 (Supporting Information) display the TEM details of the slices, where the magnetite part are composed of several nanocrystals with size of about 20–30 nm which is larger than that of nanocrystals (10 nm) in Figure 1a due to the overgrowth during annealing. The composition of the slice was measured by energy dispersive spectrum (EDS), where Fe, O, and Zr elements were confirmed (Figure 1d, inset). Figure 1e displays further the selected area electron diffraction and the EDS mapping. The lattice spacings from the polycrystalline rings match well with the known diffraction data of cubic Fe_3O_4.[27] A detailed comparison is presented in Table S1 of the Supporting Information. By elemental mapping, Fe element is found to be located in the central area, the periphery of which is surrounded by Zr element as shown in Figure 1e. Little Zr is found in the central area. Note that the light spots in the center should be caused by inevitable pollution during the cutting processes (Figure S4, Supporting Information). The O element exists within the whole region of the slice. Therefore, we can confirm that the ZrO_2 shell is distributed mainly on the surface of Fe_3O_4 supraparticles.

To clarify the influence of the ZrO_2 shell on the MR of magnetite supraparticles, different shells were synthesized by fine controlling molar ratio of the reactants with the same batch of Fe_3O_4 particles. The specific reaction parameters are listed in Table S2 of the Supporting Information, where Zr content x was tuned from 0 to 0.22 based on EDS molar ratio of the element.

The variation of Zr content in $Fe_3O_4@xZrO_2$ was probed by XRD (Figure 3a), showing two different sets of peaks based on the standard peak of Fe_3O_4 magnetite (JCPDS file No. 19–0629) and ZrO_2 (JCPDS file No. 49–1642). The pattern of pure Fe_3O_4 consists of six diffraction peaks at $2\theta \approx 30.1$, 35.4, 43.1, 53.4, 56.9, and 62.5°, respectively, which correspond to the (220), (331), (400), (422), (511), and (440) planes. According to the Debye–Scherrer's formula,[26] the average grain size of the annealed Fe_3O_4 supraparticles is estimated to be 27 nm, which is consistent with the results from TEM (Figure 1d). From the XRD patterns of the nanocomposites, two new peaks at $2\theta \approx 49.8$ and 59.8° appear with the increase of the Zr molar ratio, which matches well with the (220) and (311) planes of the ZrO_2 crystal. It can also recognize that there are two overlapping peaks at $2\theta \approx 30.1°$, which should match with the Fe_3O_4 (220) plane and ZrO_2 (111) plane, respectively. Besides that, there are no other peaks indicating good purity of the products.

It must be mentioned that γ-Fe_2O_3 has the same cubic inverse spinel structure and nearly the same lattice parameter with Fe_3O_4, and in most cases they cannot be distinguished only by XRD and TEM. Raman spectroscopy can probe the different oxide phases unambiguously. Magnetite has a main peak centered at 670 cm^{-1} (A_{1g}),[28,29] whereas maghemite (γ-Fe_2O_3) shows broad peaks around 720 cm^{-1} (A_{1g}).[30] Our results showed that only a main peak at 670 cm^{-1} was detected on both samples of the pure Fe_3O_4 and the $Fe_3O_4@xZrO_2$ as illustrated in Figure 3b, which confirm the formation of Fe_3O_4 rather than γ-Fe_2O_3.

The oxidation state of Fe at the surfaces of the samples was also investigated by XPS. Figure 3c shows the Fe-2p XPS spectrum of the pure Fe_3O_4 and the $Fe_3O_4@xZrO_2$. The XPS pattern reveals that the binding energy values of Fe $2p_{3/2}$ and Fe $2p_{1/2}$ are 710.8 and 724.6 eV, respectively, close to the reported values about Fe_3O_4 nanoparticles.[31,32] Furthermore, the absence of the

**ADVANCED
SCIENCE NEWS**
www.advancedsciencenews.com

**ADVANCED
MATERIALS
INTERFACES**
www.advmatinterfaces.de
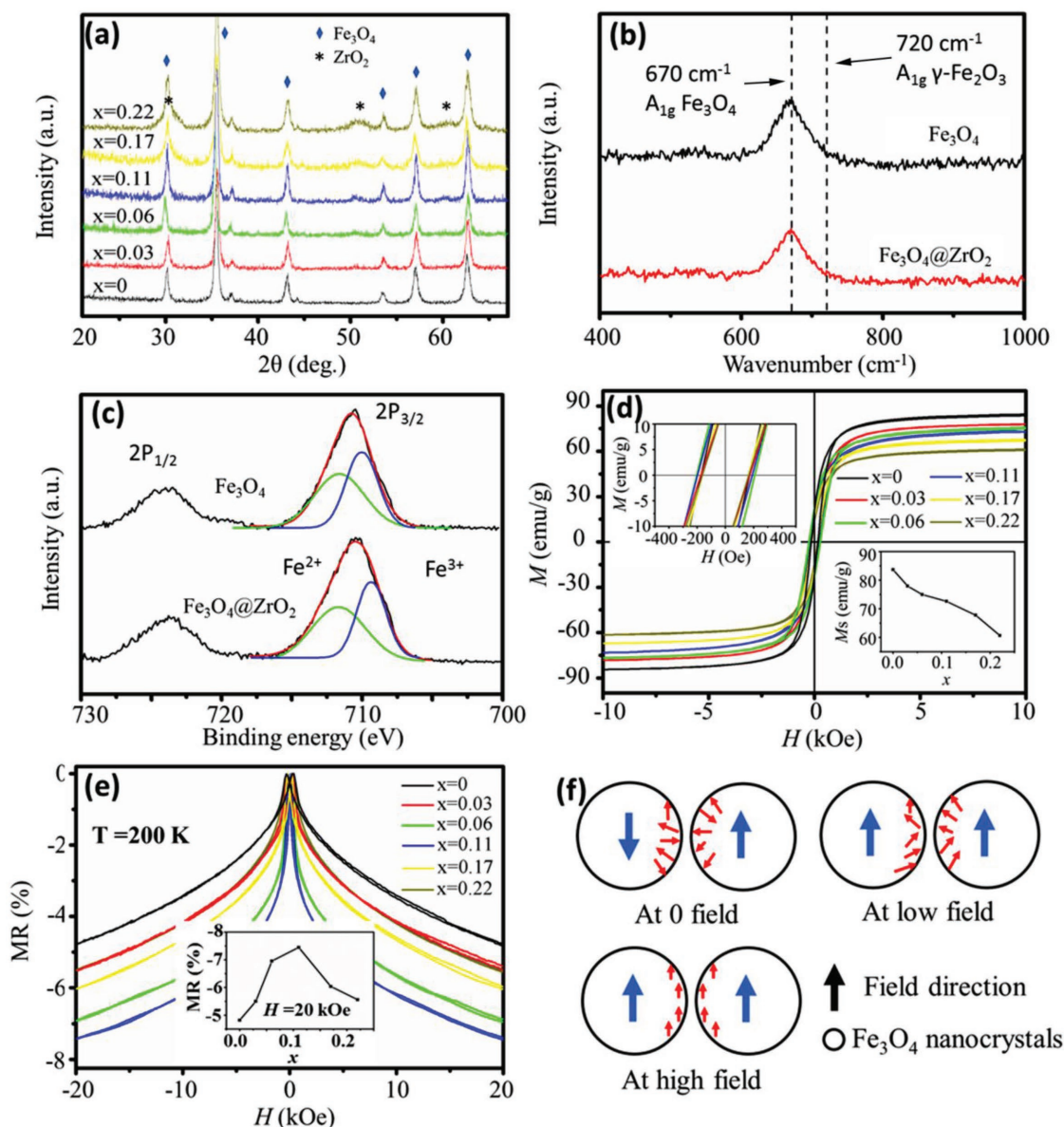
Figure 3. The effect of shell-layer on the magnetoresistance (MR) of the $Fe_3O_4@xZrO_2$ nanocomposites. a) The XRD patterns of the nanocomposites. b) The Raman spectroscopy and c) XPS spectrum of the pure Fe_3O_4 and $Fe_3O_4@xZrO_2$, $x = 0.22$. d) The saturation hysteresis loops at room temperature, the insets showing the details of the coercive field near zero field and the variation of the saturation magnetization M_s with respect to Zr molar ratio, x. e) The magnetoresistance variations with respect to magnetic field at temperature 200 K. The inset is the MR dependence on x at magnetic field 20 kOe. f) The interaction relationship between the surface spin orientation and the MR of nanoparticles system.

satellite peaks at 719.0 eV further identifies that the nanoparticles are Fe_3O_4 but not γ-Fe_2O_3. The fitting peaks at 709.0 and 711.0 eV, corresponding to the binding energy of Fe^{2+} and Fe^{3+}, respectively, is calculated to indicate that Fe^{2+}/Fe^{3+} area ratio of $Fe_3O_4@xZrO_2$ is 0.34:0.66, which is consistent with the stoichiometry of Fe_3O_4 denoted also as $FeO \cdot Fe_2O_3$. The Fe^{2+}/Fe^{3+} area ratio of pure Fe_3O_4 is 0.39:0.61, indicating the surface is oxidized slightly. The above results indicate that the existent of ZrO_2 shell could prevent oxidation of the Fe_3O_4 in some extent.

Figure 3d shows further the field dependence of intensity of magnetization of the different $Fe_3O_4@ZrO_2$ at room temperature. Typical hysteresis loops with saturation field around

3 kOe are found for all samples. The saturation magnetization (M_s) is 84 emu g^{-1} for pure Fe_3O_4 sample ($x = 0$) which is close to the bulk magnetite (92 emu g^{-1}). After coating with ZrO_2, M_s decreases monotonically with the increase of Zr content as shown in Figure 3b, bottom inset. The decrease is due to the reduction of mass fraction of ferromagnetic component in the $Fe_3O_4@xZrO_2$. Nevertheless, all samples demonstrate well ferromagnetic behavior due to the same coercivity (H_c) at around 200 Oe as shown in Figure 3b, top inset. Figure 3e shows the field dependence of MR, defined as $(\rho_H-\rho_0)/\rho_0$, where ρ_0 and ρ_H are the resistivity under zero field and applied field, respectively, measured at a fixed temperature 200 K. The DC magnetic field

is applied parallel to the current ($I//H$). The pure Fe_3O_4 MR of 4.7% is found to be lower than that of $Fe_3O_4@xZrO_2$ (x > 0). It indicates that the MR effect is obviously enhanced by adding the ZrO_2 shell layer. Butterfly-like MR curves are obtained, and the maximum MR appears at 200 Oe which is corresponding to the H_c field in the hysteresis loops (Figure 3d inset). With the increase of molar ratio x, the MR increases first and then decreases, as shown in Figure 3e, inset. The maximum of MR is 7.5% at $x = 0.11$, which corresponds to 56% raise to that of the pure Fe_3O_4. The variation of MR indicates that the addition of ZrO_2 insulator layer promotes the formation of electron tunneling, while an overthick layer with large barrier increase the difficulty of electron tunneling and then decreases the MR of the particles system. Further, Figure 3e gives that the MR climbs quickly around the H_c field and then become slow to the high field, and interestingly is not saturated even reach to the maximum field 20 kOe in spite that the saturation magnetic field is only 3 kOe (Figure 3d). This indicates that the measured MR-H curves do not accord with the relationship of non-interacting granular system MR $\propto (M/M_s)^2$,[33,34] with which M should be M_s at $H \geq 3$ kOe in our system and MR should

be a constant. In fact, the spin disordering of particles surface, originated from the symmetry broken, make the MR very hard to reach the completed saturation, even the spin of particles at central part have oriented orderly at the field direction. In this situation, the saturated MR could be reached only if the spins at the particles surface all orient at the same direction with very high magnetic field.[35,36] This explanation is described schematically in Figure 3f.

The temperature (T) dependence of resistivity (ρ) of the $Fe_3O_4@xZrO_2$ at the optimized value $x = 0.11$ is shown in **Figure 4**a, where the resistivity increases as the temperature decreases from 300 to 100 K. According to the SHENG model,[33,37] if conduction mechanism is the electron tunneling between adjacent grains, the conductivity satisfy the expression as $\sigma_m \propto \exp[-2(C/kT)^{1/2}]$, where C is a constant, k is Boltzmann's constant, and T is temperature. Thus, the logarithmic resistivity should be proportional linearly to $T^{-1/2}$. Figure 4a inset presents the characteristic linear relationship between $\ln \rho$ and $T^{-1/2}$, which indicates that the conductance mechanism is a typical grain-boundary electron-tunneling.
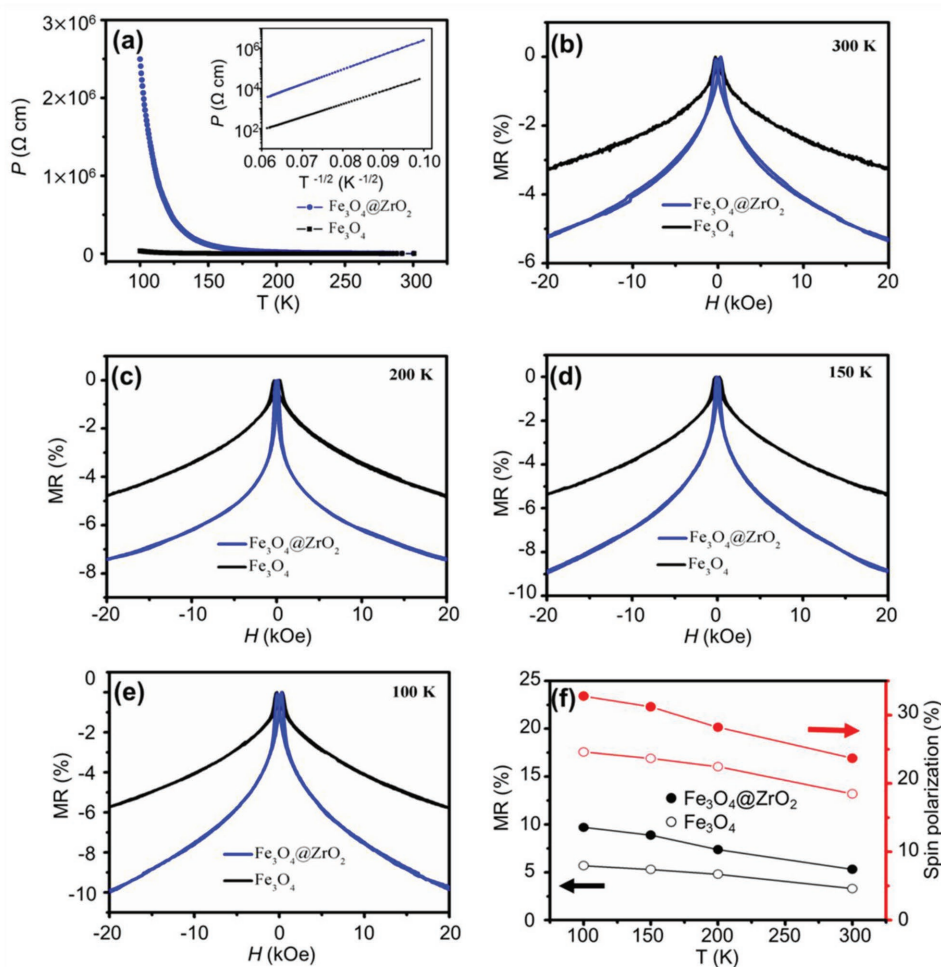
Figure 4. The MR as a function of temperature and magnetic field for the pure Fe_3O_4 and $Fe_3O_4@xZrO_2$, $x = 0.11$. a) The relationship of resistivity and temperature. The inset shows the relationship of $\ln\rho$ versus $T^{-1/2}$. b–e) The MR as a function of applied field at temperatures of 300, 200, 150, 100 K, respectively. f) The temperature dependence of the MR and the spin polarization.

**ADVANCED
SCIENCE NEWS**

www.advancedsciencenews.com

**ADVANCED
MATERIALS
INTERFACES**

www.advmatinterfaces.de

The field dependence of MR ratio for the sample of $x = 0.11$ at temperature of 300, 200, 150, 100 K, respectively, was investigated (Figure 4b–e). At 300 K, the MR value reaches about 5.1%, which is 55% larger than that of pure Fe_3O_4 of 3.3% as shown in Figure 4b. With the decrease of temperature, the difference of MR increases between the $Fe_3O_4@ZrO_2$ and the pure Fe_3O_4. As the temperature drops to 100 K, the MR increases to 9.7%, which is 70% larger than that of pure Fe_3O_4 (Figure 4e). The temperature dependence of MR is summarized in Figure 4f, black curves. The increase trend of MR with reduced temperature can be attributed to the spin mixing effect due to the coupling between the spin-up electrons and spin-down electrons at temperatures above absolute zero. According to Helman's theory, the MR in granular systems can be expressed as

$$MR = -(JP/4kT)\left[m^2(H,T) - m^2(0,T)\right] \tag{1}$$

where J is spin exchange constant, P is spin polarization, and k is Boltzmann's constant.[38] In $T > 100$ K, the trend of MR is increased with decrease of T, which agrees well with our experimental results. By calculating P using MR $= P^2/(P^2+1)$ for the granular system,[39] the T dependence of P has the same variation trend with that of the MR-T curves as shown in Figure 4f, red lines. The maximum P of $Fe_3O_4@ZrO_2$ is 31% at 100 K, larger than that of the pure Fe_3O_4 24%. The same change is found in $Fe_3O_4@xZrO_2$ with $x = 0.22$ (Figure S5, Supporting Information).

To further clarify the MR dependence of the $Fe_3O_4@ZrO_2$ on the core-size, the supraparticles with different sizes were prepared by subtly adjusting the content of reactants $FeCl_3$, as shown in **Figure 5**a–c. The average diameters of the supraparticles are 144 ± 13.5, 244 ± 22.4, and 349 ± 10.5 nm, respectively (Figure 5a–c inset). All of the supraparticles were coated with the same content of ZrO_2 ($x = 0.03$). Figure 5d and inset show the obtained MRs-H curves, indicating that the MR rises monotonically with the decrease of the Fe_3O_4 core-size. According to Xiao's theory,[40] the MR is inversely proportional to the particles diameter, that is MR$\propto 1/d_m$, where d_m is the diameter of particles. The inverse relation is confirmed by our experiments, and the increase of MR may attribute to an increase of specific surface area with the decrease of the particles size, and correspondingly an increased probability of the electron tunneling.

3. Conclusions

In summary, the core–shell nanocomposites of $Fe_3O_4@ZrO_2$ with controllable shell thickness and core dimensions have been prepared successfully. The effect of shell thickness and core size on MR properties has been investigated. The MR value of $Fe_3O_4@ZrO_2$ is much larger than that of pure Fe_3O_4. With the temperature decreasing, the MR of $Fe_3O_4@ZrO_2$ monotonically increases, which is attributed to the spin mixing behaviors. With the increase of shell thickness, the MR increases first and then decreases. The maximum of MR is 7.5% at the molar ratio $x = 0.11$, 56% larger than that of the pure Fe_3O_4. It means that the barrier induced by the ZrO_2 insulator is a crucial factor for the formation of large MR effect. However, an over-thick insulator layer will lead to the excessive barrier, decreasing and even blocking the electron tunnelings. Also, $Fe_3O_4@ZrO_2$ with different core-size show that the MR rises monotonically with
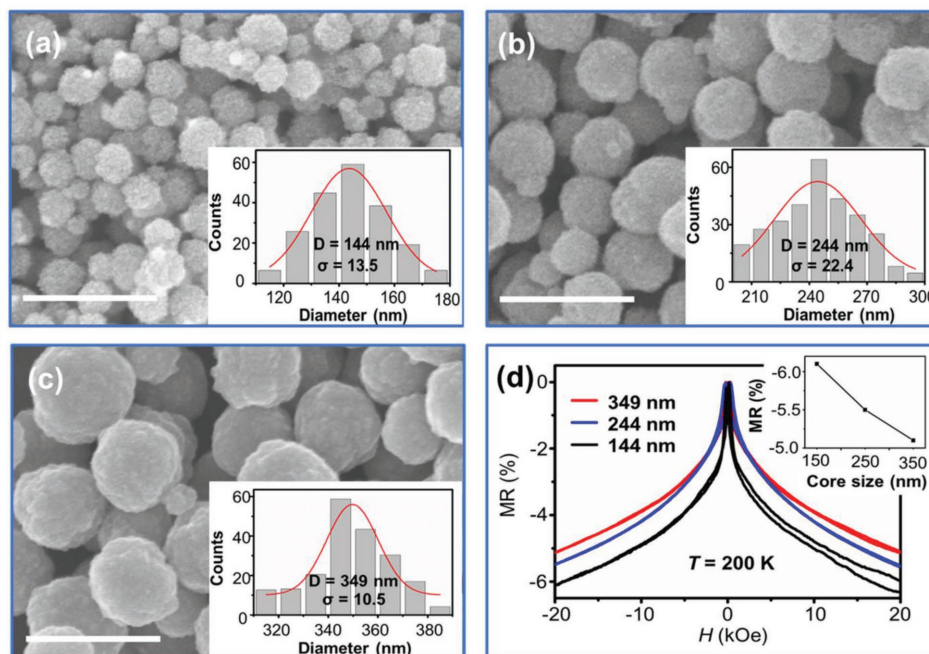
Figure 5. The influence of core size on the MR of the $Fe_3O_4@xZrO_2$ nanocomposites. a–c) SEM images showing the $Fe_3O_4@ZrO_2$ with different core size. The inset is the size distribution of the supraparticles and the lognormal fittings. d) The MR-H curves showing the effect of core-size of the $Fe_3O_4@ZrO_2$ on the MR, the inset is the variation curve of the core size and MR at magnetic field 20 kOe. The scale bar is 500 nm.

a decrease of the core-size. This may attribute to the increase of the specific surface area, which leads to the increase of electron tunneling probability. These findings will have important impacts both from the fundamental science perspective and the desirable practical application perspective.

4. Experimental Section

Materials: $FeCl_3$, zirconium isopropoxide and ethylene glycol were purchased from Alfa Aesar, USA. Trisodium citrate and NaAc were purchased from Beijing Chemical Reagents Company, China. All reagents were analytical grade and used without any further purification.

Preparation of Fe_3O_4 Supraparticles: The monodisperse Fe_3O_4 nanospheres were synthesized by solvothermal reduction method using $FeCl_3$ as starting precursor.[41] 0.9 g $FeCl_3$, 1.2 g trisodium citrate, and 3.8 g NaAc were dissolved in 50 mL ethylene glycol under vigorous stirring for 45 min. Then the solution sealed in a 100 mL Teflon-lined stainless-steel autoclave and maintained at 210 °C for 12 h. After that, let the autoclave cooled naturally to the room temperature. The as-prepared magnetite nanoparticle was collected by magnetic separation and then cleaned by ethanol for several times to remove the remaining surfactant polyethylene glycol. The average size of the particle is ≈260 nm in diameter.

Preparation of Fe_3O_4@ZrO_2 Core–Shell Nanoparticles: The ZrO_2-coated Fe_3O_4 composites were prepared using sonochemical approach.[42] 0.25 g Fe_3O_4 was added to a solution obtained by dissolving 0.1 g of zirconium isopropoxide in 50 mL ethanol, and the solution was ultrasonicated for 30 min. Then, a 1:5 (v/v) mixture of water and ethanol was added dropwise under sonicating for 2 h. The product was collected by magnetic decantation and repeatedly washed with ethanol. The obtained particles were subsequently annealed in pure Argon atmosphere for 1.5 h at 450 °C. Part of the samples was then cold pressed into pellets under pressure of 1000 MPa.

Fault-Cutting Experiments of the Fe_3O_4@ZrO_2 Nanoparticles: For the fault-cutting parts, the deposited Fe_3O_4@ZrO_2 samples were immersed first into epoxy resin embedding agent with a suitable mixing ratio, then let the embedding agent solidify. After that, trim the sample carefully with a fine surface for the next slicing. The cutting steps were carried out on a Leica UC7 ultramicrotome with a diamond blade. The thickness of the samples was kept at around 50 nm. After that, the slices were dispersed into methanol and fished quickly onto a duplex copper grid for preventing as much as possible the destruction of the magnetic nanoparticles to the TEM equipment. The TEM observations were performed on an FEI Tecnai G2 F30 microscopy at 300 kV.

Characterizations: The XRD patterns were obtained on a Rigaku D/max2200PC using monochromatic Cu-Kα radiation (40 kV, 40 mA). TEM was performed on a JEM-2100 operating at an accelerating voltage of 200 kV or on an FEI Tecnai G2 F30 microscopy at 300 kV. The Raman spectra were collected by Jobin Yvon Lab RAM HR800 Raman instrument using excitation light source of wavenumber 633 nm. XPS measurements were performed in a Thermo Escalab 250XI instrument with a hemispheric analyzer using monochromatized Al Kα photons (1486.6 eV). The binding energy scales of the spectra were aligned through the C1s peak (284.8 eV). Scanning electron microscopy (SEM) was performed on a Hitachi S-4800 microscope operating at 10 kV. The magnetization curves were measured using a vibrating sample magnetometer with a maximum field of 10 kOe. Magnetoresistance was characterized by a Quantum-Design PPMS-14H equipment. The resistance was measured by the standard 4-contacts technique with current parallel to the magnetic field.

Supporting Information

Supporting Information is available from the Wiley Online Library or from the author.

Conflict of Interest

The authors declare no conflict of interest.

[1] T. S. Herng, W. Xiao, S. M. Poh, F. Z. He, R. Sutarto, X. J. Zhu, R. W. Li, X. Yin, C. Diao, Y. Yang, X. Huang, X. Yu, Y. P. Feng, A. Rusydi, J. Ding, *Nano Res.* **2015**, *8*, 2935.

[2] Z. Zhang, S. Satpathy, *Phys. Rev. B* **1992**, *44*, 13319.

[3] W. Xiao, W. D. Song, T. S. Herng, Q. Qin, Y. Yang, M. Zheng, X. L. Hong, Y. P. Feng, J. Ding, *Nanoscale* **2016**, *8*, 15737.

[4] I. C. Lekshmi, R. Buonsanti, C. Nobile, R. Rinaldi, P. D. Cozzoli, G. Maruccio, *ACS Nano* **2011**, *5*, 1731.

[5] Y. S. Dedkov, U. Rudiger, G. Guntherodt, *Phys. Rev. B* **2002**, *65*, 064417.

[6] D. H. Zhang, Z. Q. Liu, S. Han, C. Li, B. Lei, M. P. Stewart, J. M. Tour, C. W. Zhou, *Nano Lett.* **2004**, *4*, 2151.

[7] J. D. Coey, A. E. Berkowitz, L. Balcells, F. F. Putris, F. T. Parker, *Appl. Phys. Lett.* **1998**, *72*, 734.

[8] A. Tkach, M. B. Yazdi, M. Foerster, F. Buttner, M. Vafaee, M. Fries, M. Klaui, *Phys. Rev. B* **2015**, *91*, 024405.

[9] K. P. McKenna, F. Hofer, D. Gilks, V. K. Lazarov, C. L. Chen, Z. C. Wang, Y. Ikuhara, *Nat. Commun.* **2014**, *5*, 5740.

[10] T. Tsuchiya, K. Terabe, M. Chi, T. Higuchi, M. Osada, Y. Yamashita, S. Ueda, M. Aono, *ACS Nano* **2016**, *10*, 1655.

[11] H. C. Wu, C. O. Coileain, M. Abid, O. Mauit, A. Syrlybekov, A. Khalid, H. J. Xu, R. Gatensby, J. J. Wang, H. J. Liu, L. Yang, G. S. Duesberg, H. Z. Zhang, M. Abid, I. V. Shvets, *Sci. Rep.* **2015**, *5*, 15984.

[12] Z. M. Liao, H. C. Wu, J. J. Wang, G. L. W. Cross, S. Kumar, I. V. Shvets, G. S. Duesberg, *Appl. Phys. Lett.* **2011**, *98*, 197.

[13] X. M. Zhang, S. Mizukami, T. Kubota, Q. L. Ma, M. Oogane, H. Naganuma, Y. Ando, T. Miyazaki, *Nat. Commun.* **2013**, *4*, 1392.

[14] S. Mi, R. Liu, Y. Y. Li, Y. Xie, Z. Y. Chen, *J. Magn. Magn. Mater.* **2017**, *428*, 235.

[15] J. Chen, X. C. Ye, S. J. Oh, J. M. Kikkawa, C. R. Kagan, C. B. Murray, *ACS Nano* **2013**, *7*, 1478.

[16] P. A. Kumar, S. Ray, S. Chakraverty, D. D. Sarma, *Appl. Phys. Lett.* **2013**, *103*, 102406.

[17] S. Kohiki, T. Kinoshita, K. Nara, K. A. Hasegawa, M. Mitome, *ACS Appl. Mater. Interfaces* **2013**, *5*, 11584.

[18] S. Chandra, R. Das, V. Kalappattil, T. Eggers, C. Harnagea, R. Nechache, M. H. Phan, F. Rosei, H. Srikanth, *Nanoscale* **2017**, *9*, 7858.

**ADVANCED
SCIENCE NEWS**

www.advancedsciencenews.com

**ADVANCED
MATERIALS
INTERFACES**

www.advmatinterfaces.de

[19] J. F. Wang, J. Shi, D. C. Tian, H. Deng, Y. D. Li, P. Y. Song, C. P. Chen, *Appl. Phys. Lett.* **2007**, *90*, 213106.

[20] S. Wang, F. J. Yue, D. Wu, F. M. Zhang, W. Zhong, Y. W. Du, *Appl. Phys. Lett.* **2009**, *94*, 012507.

[21] X. Z. Wang, L. S. Wang, Q. F. Zhang, X. Liu, J. Xie, A. M. Su, H. F. Zheng, D. L. Peng, *J. Magn. Magn. Mater.* **2017**, *438*, 185.

[22] E. Liu, H. L. Yuan, Z. X. Kou, X. M. Wu, Q. Y. Xu, Y. Zhai, Y. X. Sui, B. A. You, J. Du, H. R. Zhai, *Sci. Rep.* **2015**, *5*, 11164.

[23] Y. Jin, X. P. Cui, Y. Z. Gao, Y. F. Fang, B. Lu, S. X. Cao, J. C. Zhang, *Solid State Commun.* **2015**, *215*, 12.

[24] G. Lalitha, D. Das, D. Bahadur, P. V. Reddy, *J. Alloy Compd.* **2008**, *464*, 6.

[25] W. J. Lu, Y. P. Sun, X. B. Zhu, W. H. Song, J. J. Du, *Mater. Lett.* **2006**, *60*, 3207.

[26] P. I. P. Soares, A. M. R. Alves, L. C. J. Pereira, J. T. Coutinho, I. M. M. Ferreira, C. M. M. Novo, J. P. M. Borges, *J. Colloid Interface Sci.* **2014**, *419*, 46.

[27] S. H. Sun, H. Zeng, D. B. Robinson, S. Raoux, P. M. Rice, S. X. Wang, G. X. Li, *J. Am. Chem. Soc.* **2004**, *126*, 273.

[28] O. N. Shebanova, P. Lazor, *J. Raman Spectrosc.* **2003**, *34*, 845.

[29] Y. V. Kolen'ko, M. Banobre-Lopez, C. Rodriguez-Abreu, E. Carbo-Argibay, A. Sailsman, Y. Pineiro-Redondo, M. F. Cerqueira, D. Y. Petrovykh, K. Kovnir, O. I. Lebedev, J. Rivas, *J. Phys. Chem. C* **2014**, *118*, 8691.

[30] Y. E. Mendili, J. F. Bardeau, N. Randrianantoandro, A. Gourbil, J. M. Greneche, A. M. Mercier, F. Grasset, *J. Raman Spectrosc.* **2011**, *42*, 239.

[31] X. B. Hu, M. H. Ma, M. Q. Zeng, Y. Y. Sun, L. F. Chen, Y. H. Xue, T. Zhang, X. P. Ai, R. G. Mendes, M. H. Rümmeli, L. Fu, *Appl. Mater. Interfaces* **2014**, *6*, 22527.

[32] J. Su, M. H. Cao, L. Ren, C. W. Hu, *J. Phys. Chem. C* **2011**, *115*, 14469.

[33] J. Q. Xiao, J. S. Jiang, C. L. Chien, *Phys. Rev. Lett.* **1992**, *68*, 3749.

[34] Z. L. Lu, M. X. Xu, W. Q. Zou, S. Wang, X. C. Liu, Y. B. Lin, J. P. Xu, Z. H. Lu, J. F. Wang, L. Y. Lv, F. M. Zhang, Y. W. Du, *Appl. Phys. Lett.* **2007**, *91*, 102508.

[35] D. L. Peng, T. Asai, N. Nozawa, T. Hihara, K. Sumiyama, *Appl. Phys. Lett.* **2002**, *81*, 4598.

[36] C. Park, Y. Peng, J. Zhu, D. E. Laughlin, R. M. White, *J. Appl. Phys.* **2005**, *97*, 10C303.

[37] M. Ziese, R. Hohne, H. C. Semmelhack, H. Reckentin, N. H. Hong, P. Esquinazi, *Eur. Phys. J. B* **2002**, *28*, 415.

[38] J. Helman, B. Abeles, *Phys. Rev. Lett.* **1976**, *37*, 1429.

[39] J. Inoue, S. Maekawa, *Phys. Rev. B* **1996**, *53*, 11927.

[40] G. Xiao, J. Q. Wang, P. Xiong, *IEEE. Trans. Magn.* **1993**, *29*, 2694.

[41] J. Liu, Z. K. Sun, Y. H. Deng, Y. Zou, C. Y. Li, X. H. Guo, L. Q. Xiong, Y. Gao, F. Y. Li, D. Y. Zhao, *Angew. Chem., Int. Ed. Engl.* **2009**, *48*, 5875.

[42] H. P. Peng, R. P. Liang, L. Zhang, J. D. Qiu, *Electrochim. Acta* **2011**, *56*, 4231.